

## Improving PET With HD•PET + Time of Flight

*Michael E. Casey, Ph.D, Director of Physics, Siemens Molecular Imaging*

[www.siemens.com/mi](http://www.siemens.com/mi)

**SIEMENS**

# Improving PET With HD•PET + Time of Flight

## Introduction

Using time of flight (TOF) information to augment image reconstruction in positron emission tomography (PET) was first proposed in the early 1980's soon after the invention of PET. [1,2,3] While a number of TOF PET systems were built and used in clinical research, [4] the availability of a suitable scintillator limited the clinical application of TOF PET [5]. The discovery of LSO now provides a scintillator with both the stopping power and time resolution to make TOF PET clinically viable [6,7].

As in conventional Positron Emission Tomography, the time of flight PET camera encircles the patient with multiple rings of radiation detectors. Each pair of detectors measures the number of positron decays that lie along the line joining them. Soon after a positron is emitted by the radiotracer, it encounters an electron, and the pair annihilates emitting two gamma rays. These gamma rays travel in nearly opposite directions until they strike the detectors. In conventional PET, a positron annihilation would be registered but its position along the path would be unknown. However, in time of flight PET, the faster detectors are able to measure the difference in the arrival time of the two gamma rays, thus estimating the position of the positron annihilation along the path. This added position information enables the reconstruction algorithm to arrive at an image with fewer iterations and less image noise.

To illustrate this improvement, consider imaging the phantom shown in Figure 1. In conventional PET, the measurement just records the fact that there was an event somewhere along the lines connecting the detectors, as shown in the top row of Figure 1. In this example, only four measurement angles were used to simplify the illustration. Each measurement has a low resolution (one pixel) along the lines and a high resolution perpendicular to the lines. From these measurements, we have four estimates of the image as shown in the middle row of Figure 1. These four estimates are added to form the final estimate shown in the bottom row of Figure 1. This example illustrates the backprojection step in filtered backprojection. A sharpening filter is then applied to recover the estimate of the original image.

The addition of time of flight information allows the placement of the events along the lines connecting the detectors. In our simple example, there are 7 regions, defined by the TOF measurements, as shown in Figure 2. Again, there are four measurement angles. The estimates to the image at each angle are still blurred along the lines of response, but each estimate is closer to the original image. When these estimates are added, the final estimate is much closer to the original image than in the conventional case. Now much less filtering is required to recover a good representation of the original image.

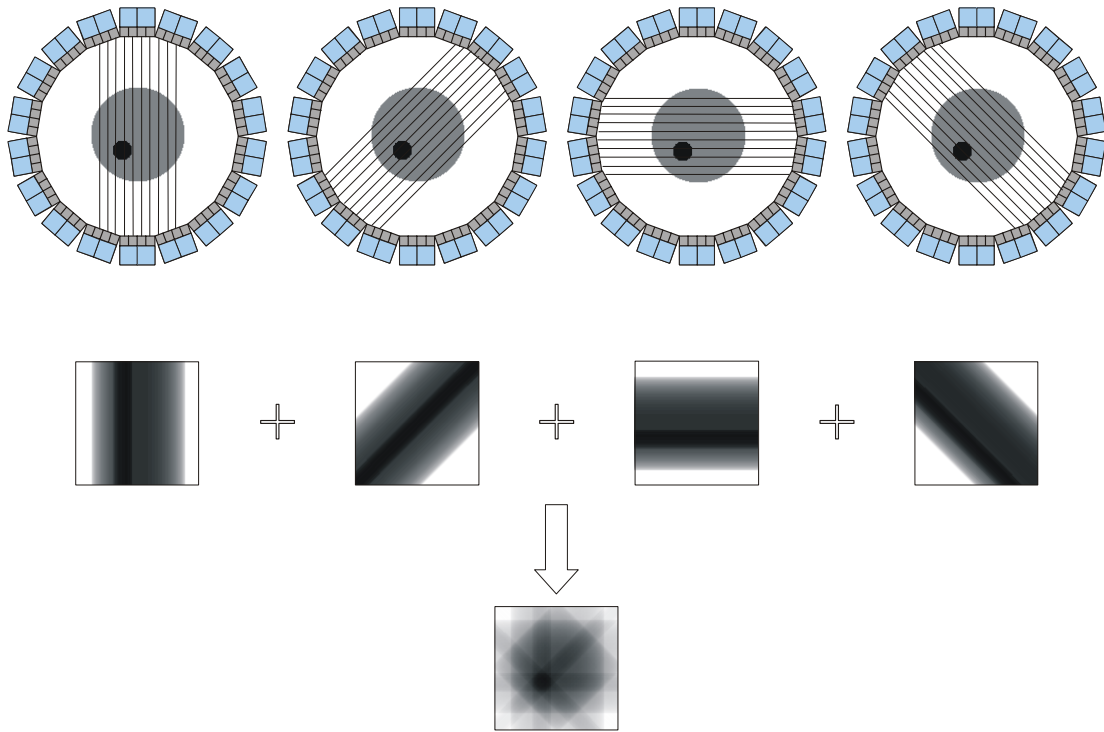


Figure 1. Data collection and reconstruction in a conventional PET scanner. (Top) Positron annihilations are collected with no position information along the lines. (Middle) Estimates of the image as seen at the measurement angle. (Bottom) Final estimate of the image is the sum of the four estimates before filtering.

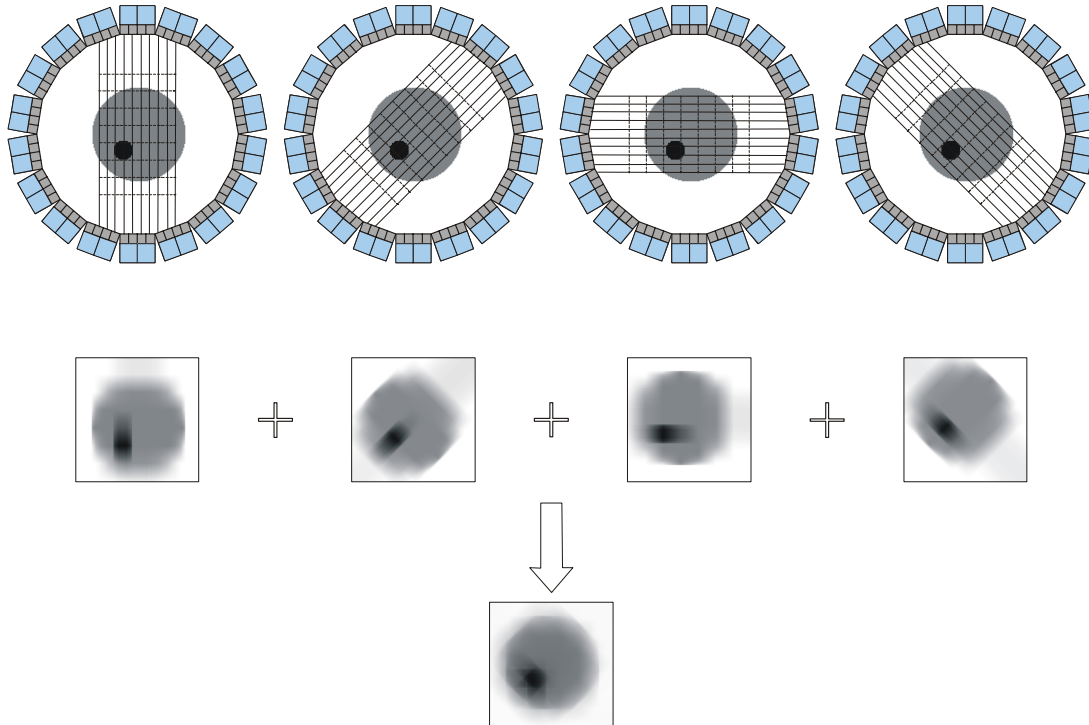


Figure 2. (Top) With TOF, data collection has position information along the lines of response. (Middle) Estimates to the image. (Bottom) Estimated image when TOF information is included.

The above example is simplistic for several reasons. The most prominent of these reasons is the absence of counting noise. When noise is present, a sharpening filter will tend to amplify the noise. Since the filter will need to extend to the edge of the image in the conventional case, the amount of noise encountered will be greater than in the TOF case. In filtered backprojection, the reduction in noise realized by including TOF information can be estimated by the simple relation:

$$Gain = \frac{Diameter\ of\ object}{Extent\ of\ filter} \quad (1)$$

Equation 1 represents the square of the gain in signal to noise ratio (SNR) obtained using TOF [2], or the gain in effective counts that would produce such noise reduction. The extent of the filter is determined by the time resolution of the system. The time resolution is the ability of the detector system to measure the difference in arrival time of the two photons. In Figure 1, the rays from the hot region in the bottom image extend to the edge of the image. In Figure 2, the rays are localized to an area around the hot region.

When a point source is placed at the center of a scanner, the distance to any detector from the source is the same. Therefore, the flight time of any two gamma rays produced by positron annihilation in the source should be the same. Yet, the inability of the detectors to measure the precise arrival will cause the measured times to differ slightly. By logging these differences one can measure the time resolution of the scanner. A reasonable measure of the time resolution of the scanner is the full-width-at-half-maximum ( $\Delta t_{FWHM}$ ) of the distribution of time differences collected from a centered source.

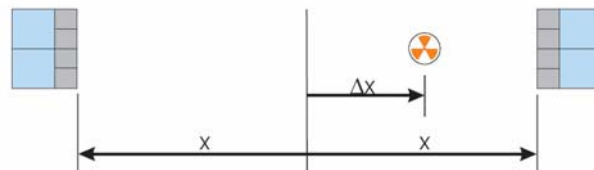


Figure 3. Source offset from center by distance  $\Delta x$ .

If the source is moved off center by a distance  $\Delta x$  as shown in Figure 3, then the average time difference measured by the two detectors is given by:

$$\Delta t = \frac{(x + \Delta x)}{c} - \frac{(x - \Delta x)}{c} = \frac{2 \cdot \Delta x}{c} \quad (2)$$

In the equation above, the symbol  $c$  is the speed of light, approximately  $3 \times 10^8$  meters per second or 30 centimeters per nanosecond. But because the source shift is added to the path of one photon and subtracted from the path of the other, a movement of the source by 15 cm causes a time difference of one nanosecond. Since the system time resolution is the ability of the system to determine the time difference, it also sets the

extent of the sharpening filter that must be applied during reconstruction. The intrinsic resolution,  $\Delta x_{\text{int}}$ , measured along the line of response using TOF information, can be a reasonable approximation of the filter extent.

$$\Delta x_{\text{int}} = \Delta t_{FWHM} \cdot \frac{c}{2} \quad (3)$$

Substituting the extent of the filter with the resolution of the system produces the classical relation for effective count gain in a TOF system when filtered backprojection image reconstruction is used:

$$\text{Gain} = \frac{\text{Diameter of object}}{\Delta t_{FWHM} \cdot \frac{c}{2}} \quad (4)$$

For a TOF PET system with a time resolution of 550 picoseconds, the resolution measured along the line of response will be 8.25 centimeters. A chart illustrating the count gain for various diameters of objects is shown in Figure 4.

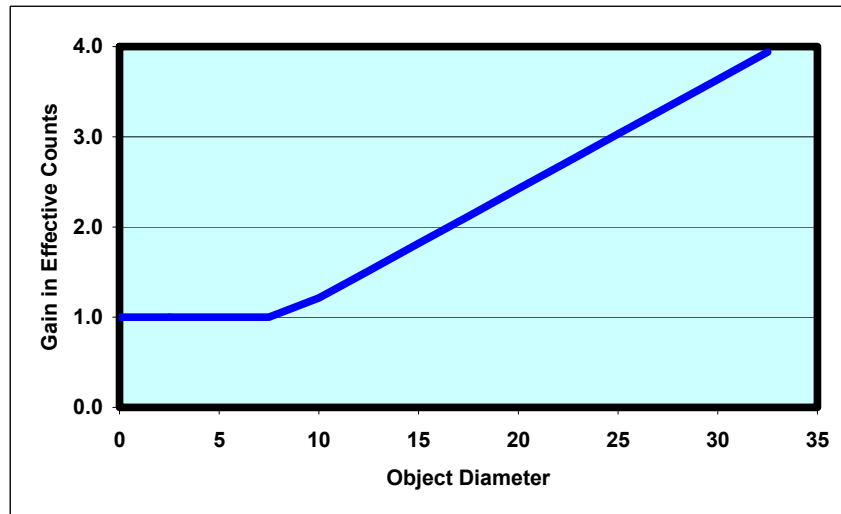


Figure 4. Gain in effective counts for a TOF PET system with a 550 picosecond time resolution.

## Iterative Reconstruction

The chart above illustrates the theoretical gain due to using time of flight information when filtered backprojection reconstruction is used. However, most clinical PET scanners use iterative reconstruction. Since iterative reconstruction algorithms such as HD•PET are non-linear, the effect of using time of flight information in the reconstruction is more complex. When TOF information is included in the reconstruction, the iterative update equation remains unchanged. However the sinogram is now divided into time bins, where each time bin contains the counts registered with a time difference of  $\Delta t$ . The iterative reconstruction works to match a sinogram simulated from a prototype image with the real sinogram. When TOF information is included, the algorithm must also simulate the time bins. Below is the iterative update equation for expectation maximization:

$$i_j^{k+1} = i_j^k \cdot \sum_i \left[ p_{i,j} \cdot \frac{s_i}{\left( \sum_j p_{i,j} \cdot i_j^k \right) + r_i + \frac{c_i}{n_i}} \right] \quad (5)$$

This equation appears complex at first glance, but the following explanation should help clarify the concepts. Basically, the update equation modifies an estimate of the image,  $i_j^k$ , with the backprojection of an error term. The error term is the measured sinogram,  $s$ , divided by a simulation of the sinogram from the image estimate. The summation in the denominator of the above equation represents the forward projection of the estimated image. Since the measured sinogram is neither normalized ( $n$ ) nor corrected for attenuation ( $a$ ), the forward projected sinogram must be divided by these corrections. Next an estimate of the random coincidences is added ( $r$ ). Finally, an estimate of the scatter ( $c$ ) is added. Since the scatter is estimated as a smooth function, it must be divided by the normalization [9].

With each iteration of the algorithm, the error term (term in square brackets in equation 5) becomes closer to unity. However, the uncertainty in the measured sinogram, caused by the low number of counts, prevents every bin in the simulated sinogram from being perfectly equal to the corresponding bin in the measured sinogram. Instead, the resulting image becomes noisy to compensate. In reality, with each iteration of the algorithm, the structures in the image approach a final value while the noise increases. The spatial information provided by the time of flight helps the algorithm because the added information allows the structures to be closer to their final value with fewer iterations. As an example, the TOF image produced by the simple example in Figure 2 is much closer to the original than the corresponding conventional image in Figure 1.

## Phantom Studies: Detectability

The ability to detect a lesion in a noisy background is one way to measure the performance of a reconstruction algorithm. An illustration of one measure of detectability similar to a non-prewhitening matched filter is shown in Figure 5. Here the contrast of the lesion or difference between the lesion and background is compared to the noise in the background. If the background noise is too large, you don't see the lesion, if the noise is low compared to the difference, you do see the lesion.

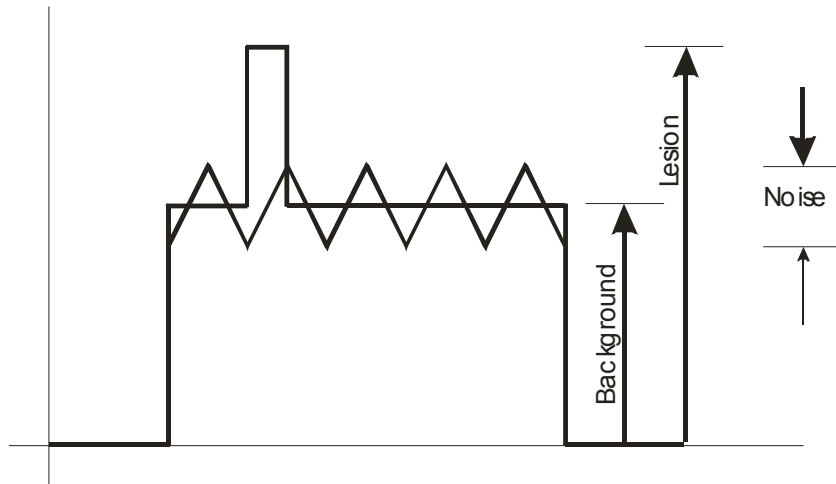


Figure 5 An idealized profile through a phantom with a hot lesion showing the parameters for a measure of detectability.

From the idealized profile in Figure 5, a measure of detectability becomes:

$$Detectability = \frac{Lesion - Background}{Noise} \quad (6)$$

In a simple experiment, the NEMA Image Quality phantom was filled with  $^{18}\text{F}$  liquid solution. The four smaller spheres (diameter 10, 13, 17, and 22 mm) were filled with a concentration 8 times the background. A representative image is shown in Figure 6 below. The two largest spheres were filled with water and contained no activity. Data was collected into a time of flight (TOF) sinogram for the TOF reconstruction and into a conventional sinogram for the conventional reconstruction. For the conventional image, the HD•PET reconstruction was used while for the TOF image, the algorithm was HD•PET with TOF extensions, from hereon referred to as ultraHD•PET. Both algorithms used 14 subsets with one to eight iterations.



Figure 6. The phantom image showing the volumes of interest used in the analysis.

Volumes of interest (VOIs) were drawn on each sphere as shown in Figure 1. The diameter of the VOI was the same as the inner diameter of the sphere. A VOI was drawn on the background as well. For the spheres, the diameter of the VOI is the same

size as the physical size of the sphere. The background VOI was a 50 mm x 100 mm cylinder.

In Figure 2 below, the mean value of the VOI drawn on each sphere was plotted as a function of the noise in the background. All the HD•PET data are blue, while the ultraHD•PET data are maroon. Iteration one is the first point on each curve and each symbol on the curve represents an additional iteration. This chart shows the VOI value increasing then asymptotically approaching a final value. At the same time, the noise increases for each new iteration. Since the VOIs are normalized to a background value of one, the values are essentially standard uptake values (SUVs). The initial sphere-to-background ratio was 8:1 but since the VOIs are drawn the same size as the physical size of the sphere, the average of the VOI will be less than 8:1. The lower recovery in the smaller spheres illustrates the effect of the finite spatial resolution and the 4 mm pixel size.

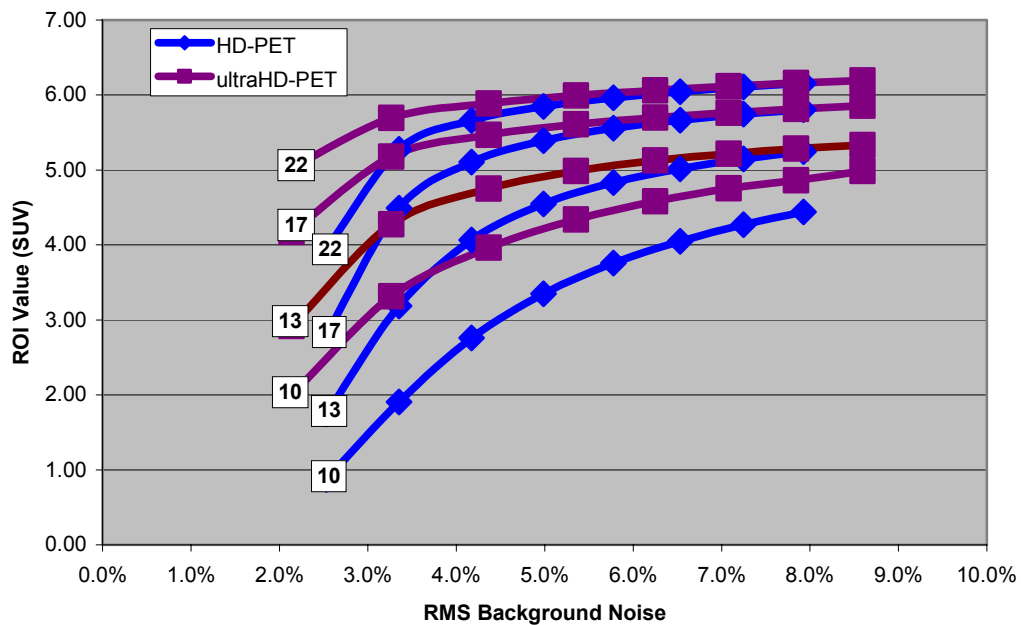


Figure 7. The mean value of the VOI plotted against the background noise.

As can be seen for both HD•PET and ultraHD•PET reconstructions, the larger spheres approach a final value in a few iterations. The smaller spheres are still significantly changing in value after 8 iterations.

Since Figure 7 shows an increase in the VOI value while the noise increases, the optimization should be to maximize the detectability. Figure 8 below shows the detectability plotted as a function of iteration. For the large spheres, the detectability decreases with each iteration. This is due to the fact that the larger structures converge quickly to their final value, and the noise continues to increase. The smaller structures take longer to reach a final value. From Figure 8, the maximum detectability for the 10 mm sphere using HD•PET reconstruction occurs at iteration 4. When ultraHD•PET is used, the maximum occurs at iteration 2. This measure allows us to set the number of iterations for the different algorithms which maximizes the detectability. Better quantification will occur with more iterations, but the detectability will suffer.

Table 1 shows the RMS background noise for both reconstruction algorithms. The HD•PET at iteration 4 shows a background noise of 5.0% while ultraHD•PET with TOF shows a 3.3% RMS noise. The NEMA image quality phantom has a width of 30 cm and a height of 23 cm. The TOF formula, equation 4, assumes a circular phantom so averaging the width and height gives an approximate circular diameter of 26.5 cm. Then the TOF formula predicts the gain in effective counts for a system with a time resolution of 550 picoseconds to be 3.2. The observed gain changes as the square of the noise ratio, or  $(5\%/3.3\%)^2 = 2.3$ .

For the two reconstruction algorithms, HD•PET iteration 4, and ultraHD•PET iteration 2, the detectability of all the spheres is greater for the ultraHD•PET image.

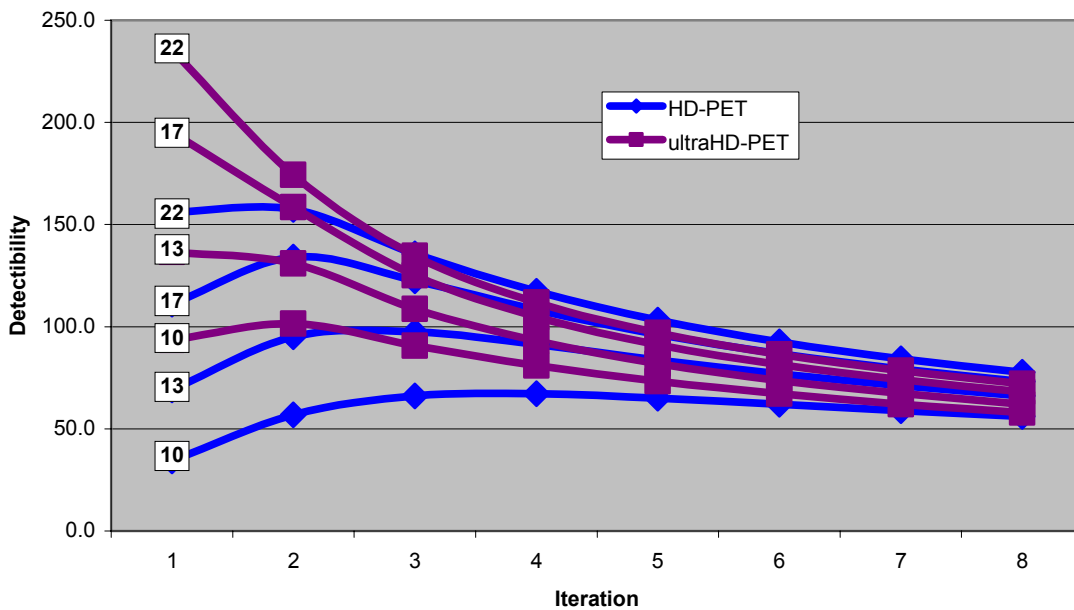


Figure 8. Detectability as a function of iteration. The number in the box at the beginning of the curve is the diameter of the sphere.

Table 1. Background noise for each iteration

Iteration	Algorithm	
	HD•PET	ultraHD•PET
1	2.5%	2.1%
2	3.4%	3.3%
3	4.2%	4.4%
4	5.0%	5.4%
5	5.8%	6.3%
6	6.5%	7.1%
7	7.2%	7.8%
8	7.9%	8.6%

## Phantom studies: human observers

In a similar experiment [10], designed to compare the performance of various reconstruction algorithms using human observers, a torso phantom was constructed where the lesions were small solid spheres of  $^{68}\text{Ge}$  and the background was  $^{18}\text{F}$ . The phantom consisted of a Hoffman 3D brain phantom for a head, an RXD thorax phantom for body and an elliptical phantom for hips. In this experiment there were 26 total lesions placed throughout the phantom. The phantom was scanned on three consecutive days at four different concentrations giving four distinct lesion-to-background ratios. Between the first and second day, the lesion positions were changed, and all lesions were removed on the third day. Figure 9 below shows maximum intensity projections of a representative pair of images from these data, reconstructed with HD•PET and ultraHD•PET.

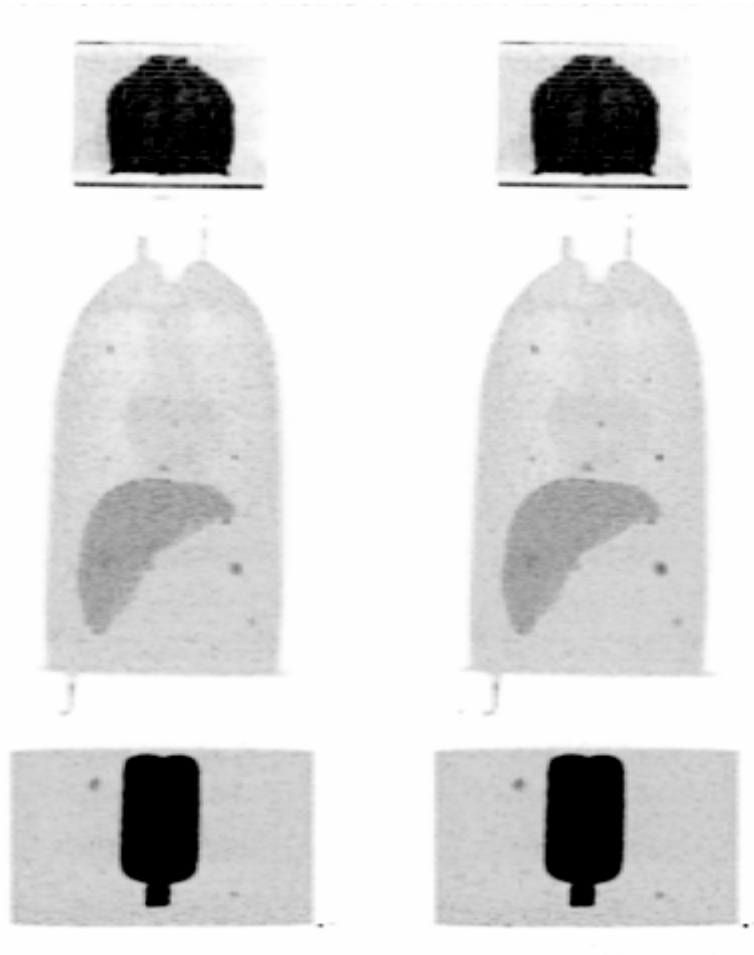


Figure 9. The torso phantom used in the human observer experiment. (Left) reconstructed with HD•PET; (Right) reconstructed with ultraHD•PET.

All the data from the scans were reconstructed with four reconstruction algorithms: OP-OSEM, HD•PET, OP-OSEM+TOF and ultraHD•PET. The ordinary Poisson

(OP-OSEM) reconstructions, and the HD•PET are similar in the fact that the Poisson nature of the data are preserved as in Equation 5 above. However, the HD•PET models the point spread function of scanner while OP-OSEM does not. To maintain the Poisson statistics, both algorithms model the non-linear sampling due to the circular detector geometry.

Each of five observers evaluated 104 test images which might or might not contain a lesion. If a lesion was suspected, the observer clicked on the lesion. When the cursor was close to a real lesion, a true positive was logged, if not, a false positive was logged.

The data from the observer study were analyzed to form receiver operating characteristic curves (ROC). This ROC analysis summarizes the performance of the observers' ability to correctly identify lesions. Of course, the quality of the reconstruction algorithm controls the observers' performance in this task. Table 2 below lists the results of the study. The column labeled  $A_{LROC}$  (area under the localization ROC curve) can be interpreted as the probability that the observer chooses an image containing a lesion and correctly localizes the lesion within the image [11]. From these results, the lesion detection ability using the ultraHD•PET algorithm performs better than HD•PET alone. The HD•PET performs better than OP-OSEM and only slightly worse than OP-OSEM+TOF.

Table 2. Results of the human observer study

	$P_{LOC}$	$A_{LROC}$
OP-OSEM	0.55	0.43
HD•PET	0.69	0.60
OP-OSEM+TOF	0.74	0.65
HD•PET+TOF	0.89	0.84

## Clinical Studies

Phantom studies are good at assessing the performance of reconstruction algorithms since the truth is known. However, the algorithms will be used clinically. Now the question becomes one of how the algorithms perform in a clinical environment. Based on the theory discussed above, one would expect an improvement in clinical images when TOF information is used in the reconstruction algorithm.

### Clinical studies: TOF gain

In this study, 46 patients were analyzed using a detectability measure similar to that illustrated in Figure 5 above [12]. For each patient data set, two images were reconstructed using HD.PET and HD.PET+TOF. In each pair of images, a lesion was selected and an ROI placed around the lesion. The liver was assumed to have uniform uptake of FDG. This assumption of uniformity allows a measure of noise to be computed by forming the standard deviation of the pixels within an ROI on the liver. So using equation 6 above, a detectability measure was computed for each reconstruction. The gain is then the ratio of the lesion detectability of the image reconstructed with HD.PET+TOF divided by the lesion detectability of the image reconstructed with HD.PET. The gain in detectability for lesions from the 46 patients is plotted as a function of body mass index (BMI) in Figure 10 below. The symbols are the measured gain while the solid line is a fit to the measurements. These lesions were all located within the

abdomen; lesions in the head and neck region and in the lung were excluded from this study. These data show a gain for all lesions when the TOF information is used and also show a trend toward higher gain for higher BMI patients. Since the gain is a ratio of two signal-to-noise ratios, this gain can be interpreted as the square root of the effective gain in counts.

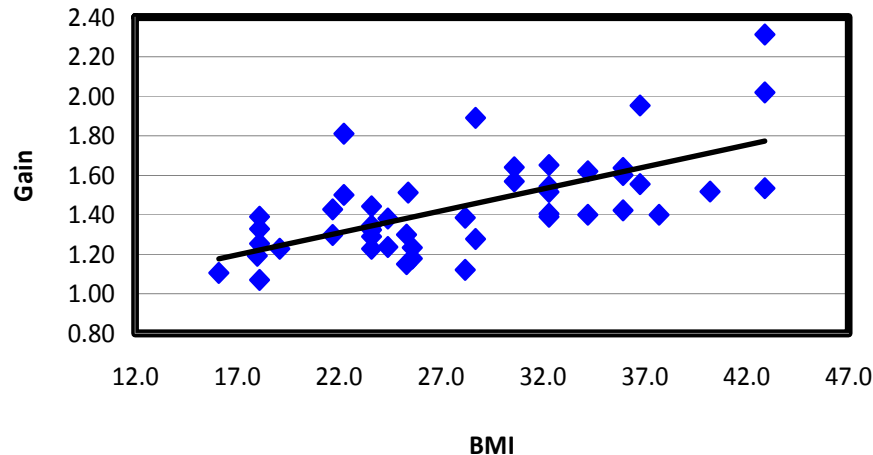


Figure 10. Gain in detectability for selected lesions in 46 clinical scans when TOF information is used in the HD.PET reconstruction. Data are represented by the symbols. The line shows a least-squares linear fit to the data.

### Clinical studies : effect of shorter scan

When using TOF information to reconstruct images, the image noise is decreased without sacrifice of contrast. Therefore, it may be possible to scan for less time when TOF information is used. Conversely, in situations where radiation dose is an issue, the possibility exists to lower the injected activity and still obtain the same quality image as can be achieved with a longer scan or higher activity without the TOF reconstruction. The experiment described in the following paragraphs supports this hypothesis.

A 178 cm patient weighing 68 kg (BMI 21.7) was injected with 10.94 mCi of  $^{18}\text{F}$  FDG 90 minutes prior to imaging. CT images were acquired for attenuation correction. For the PET, 5 bed positions of 2 minutes per bed were acquired in listmode.

For each bed position, a listmode file containing half the number of counts was built by deleting every other count in the original file. This method of reducing the counts is preferable to scanning the patient a second time in that the biology remains constant for both the long scan and the “short” scan. This “short” scan is equivalent to either an injected activity of 5.5 mCi with a scan time of 2 minutes or a 10.92 mCi injection with a scan time of 1 minute.

For both listmode scans, the images were reconstructed by three methods: 3D-AWOSEM, HD•PET and ultraHD•PET. As shown above, the different reconstruction algorithms converge at different rates. The phantom experiment described above was used as a guide to select the number of iterations and subsets necessary to obtain the

optimum image for each algorithm. Table 3 below summarizes the reconstruction parameters.

Table 3. Reconstruction parameters used in the scan time experiment.

	Iterations	Subsets	Filter
3D-AWOSEM	3	8	5mm
HD•PET	4	14	none
ultraHD•PET	2	14	none

The same assumptions were used in this experiment as described in the analysis of the 46 patients above. The uptake of FDG in the liver can be assumed to be reasonably uniform so that the pixel to pixel standard deviation can be used as a measure of image noise. The contrast is computed by placing an ROI on a small lesion and comparing the uptake in the lesion to the uptake in the liver. The detectability is defined similar to a non-prewhitening numerical observer as in equation 6. Table 4 shows the results of the ROI analysis where the ROIs drawn are shown in the patient images in Figure 11.

Table 4. The results of the ROI analysis on the one and two minute scans.

		Liver Uptake	Liver Standard deviation	Lesion Uptake	Contrast	Noise
2 Minute	3D-AWOSEM	6798.2	705.1	28847.2	3.24	10.4%
	HD•PET	6704.6	1092.9	42757.8	5.38	16.3%
	ultraHD•PET	7222.1	838.6	46687.4	5.46	11.6%
1 Minute	3D-AWOSEM	3406.1	460.8	13070.7	2.84	13.5%
	HD•PET	3298.1	744.3	20637.4	5.26	22.6%
	ultraHD•PET	3566.5	570.8	22342.2	5.26	16.0%

The rows labeled 2 minutes are from the original listmode file while the rows labeled 1 minute are from the shortened file. An examination of the contrast and noise for the one minute ultraHD•PET reveals approximately the same contrast and noise values as the 2 minute HD•PET reconstruction. For this particular patient, the improvement in TOF could be termed as equivalent to an increase in counts by a factor of two.

## Conclusions

The information provided by time of flight aids the reconstruction, producing superior image quality than can be obtained by a conventional non-TOF PET scanner. One measure of image quality as described in this paper is lesion detectability. The TOF images consistently show better lesion detectability than images reconstructed without TOF information. The human observer experiment using phantoms further supports the premise of higher detectability when TOF information is used.

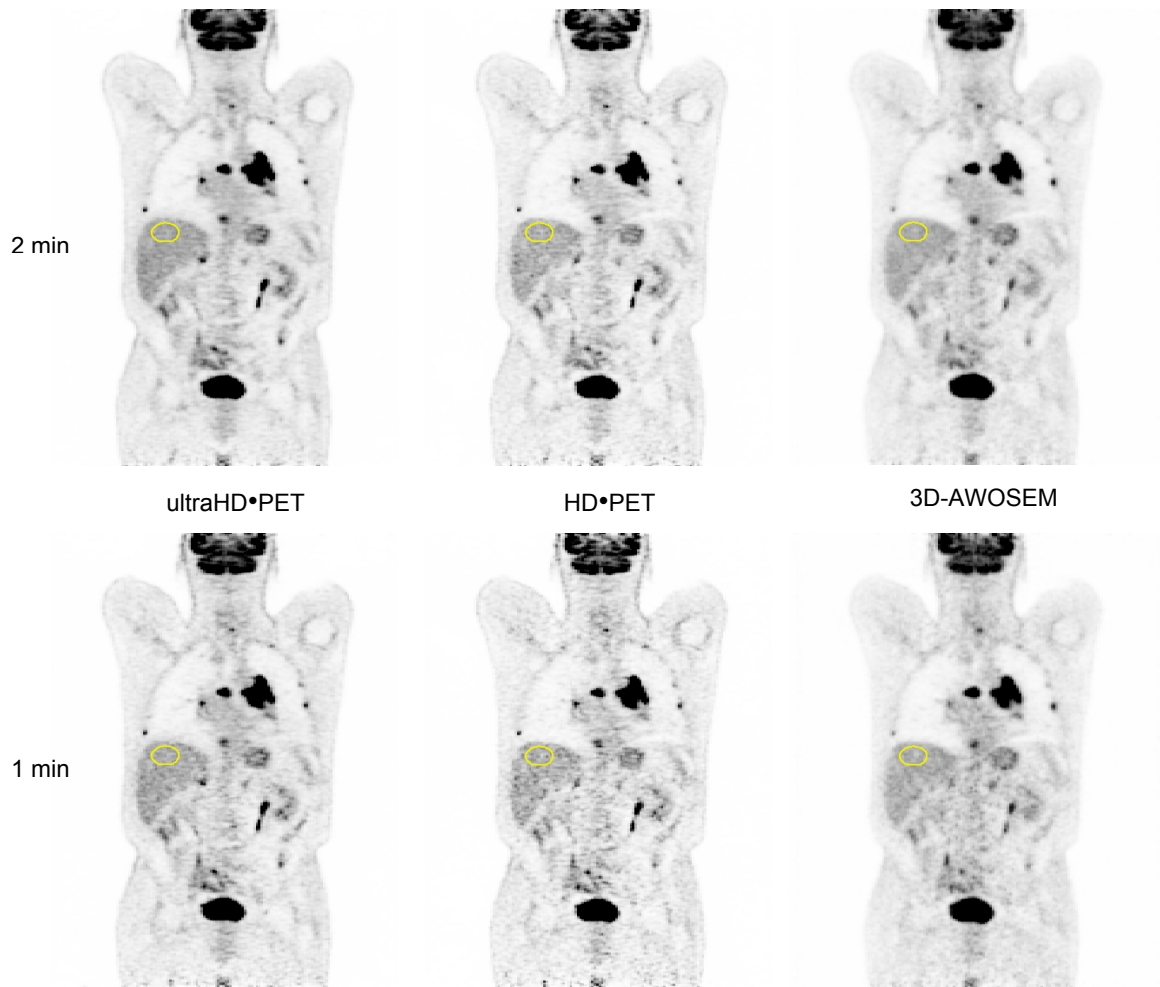


Figure 11. Patient image from listmode experiment. (Top) Original two minute scan per bed position. (Bottom) Simulated one minute per bed scan.

## References:

1. T.F. Budinger, "Instrumentation trends in nuclear medicine", *Semin.Nucl. Med.*, vol. 7, pp.285-297, 1977.
2. T.F. Budinger, "Time-of-flight positron emission tomography: status relative to conventional PET", *J. Nucl. Medicine*, vol. 24, pp. 73-78,1983.
3. N.A. Mullani, J. Markham, M.M. Ter-Pogossian, "Feasibility of time-offlight reconstruction in positron emission tomography", *Journal of Nuclear Medicine*, vol. 21, pp. 1095-97, 1980.
4. Bendriem, B., Soussaline, F., Campagnolo, R., Verrey, B., Wajenberg, P., Syrota, A.; "A Technique for Correction of Scattered Radiation in a PET System using Time-of-Flight Information", *J Computer Assist Tomogr*, 10(2) 1986; pp 287-295
5. Allemand R, Gresset C, Vacher J; "Potential advantages of a cesium Fluoride scintillator for a time-of-flight positron camera;" *J Nucl Med* 1980;21:153-5

6. Conti, M. "State of the Art and Challenges of Time-Of-Flight PET" submitted to *Physica Medica*, European Journal of Medical Physics, June 18 2008.
7. Melcher CL, and Schweitzer JS, "Cerium-doped Lutetium Oxyorthosilicate: A Fast, Efficient New Scintillator," *IEEE Trans. Nucl. Sci.*, NS-39 No. 4, pp 502-505, 1992.
8. Watson, C.C.; "Extension of Single Scatter Simulation to Scatter Correction of Time-of-Flight PET;" *IEEE Trans. Nucl. Sci.* Volume 54, Issue 5, Part 1, Oct. 2007 Page(s):1679 – 1686
9. Casey, M. E. "Point Spread Function Reconstruction in PET;" [www.siemens.com/mi](http://www.siemens.com/mi)
10. Kadrmas, D., Casey, M.E., Panin, V.; "Impact of TOF on PET tumor detection: An LROC study;" *J Nucl Med.* 2008; 49 (Supplement 1):62P
11. Swensson, R., "Unified measurement of observer performance in detecting and localizing target objects on images;" *Med. Phys.* 23 (10) Oct 1996, 1709-1725
12. Conti, M., Townsend, D., Casey, M., Lois, C., Jakoby, B., Long, M., Howe, C., Watson, C. and Bendriem, B.; "Assessment of the clinical potential of a time-of-flight PET/CT scanner with less than 600 ps timing resolution;" *J Nucl Med.* 2008; 49 (Supplement 1):411P

Trademarks and service marks used in this material are property of Siemens Medical Solutions USA or Siemens AG. All other company, brand, product and service names may be trademarks or registered trademarks of their respective holders.

Note: Original images always lose a certain amount of detail when reproduced.

All photographs © 2008 Siemens Medical Solutions USA, Inc. All rights reserved.

#### **Global Business Unit Address**

Siemens Medical Solutions USA, Inc.  
Molecular Imaging  
2501 N. Barrington Road  
Hoffman Estates, IL 60192  
USA  
Telephone: +1 847 304 7700  
[www.siemens.com/mi](http://www.siemens.com/mi)

#### **Global Siemens Headquarters**

Siemens AG  
Wittelsbacherplatz 2  
80333 Munich  
Germany

#### **Global Siemens Headquarters Healthcare Headquarters**

Siemens AG  
Healthcare Sector  
Henkestrasse 127  
91052 Erlangen  
Germany  
Telephone: +49 9131 84-0  
[www.siemens.com/healthcare](http://www.siemens.com/healthcare)

#### **Legal Manufacturer**

Siemens Medical Solutions USA, Inc.  
Molecular Imaging  
810 Innovation Drive  
Knoxville, TN 37932-2751  
USA  
Telephone: +1 865 218 2000  
[www.siemens.com/mi](http://www.siemens.com/mi)